

A Self-Limited Free-Standing Sulfide Electrolyte Thin Film for All-Solid-State Lithium Metal Batteries

Gao-Long Zhu, Chen-Zi Zhao, Hong-Jie Peng, Hong Yuan, Jiang-Kui Hu, Hao-Xiong Nan, Yang Lu, Xin-Yan Liu, Jia-Qi Huang, Chuanxin He, Jian Zhang, and Qiang Zhang*

All-solid-state (ASS) lithium metal batteries (LMBs) are considered the most promising next-generation batteries due to their superior safety and high projected energy density. To access the practically desired high energy density of ASS LMBs, an ultrathin solid-state electrolyte (SSE) film with fast ion-transport capability presents as an irreplaceable component to reduce the proportion of inactive materials in ASS batteries. In this contribution, an ultrathin (60 μm), flexible, and free-standing argyrodite ($\text{Li}_6\text{PS}_5\text{Cl}$) SSE film is designed through a self-limited strategy. A chemically compatible cellulose membrane is employed as the self-limiting skeleton that not only defined the thinness of the sulfide SSE film but also strengthened its mechanical properties. The ionic conductivity of the SSE film reaches up to $6.3 \times 10^{-3} \text{ S cm}^{-1}$ at room temperature, enabling rapid lithium-ion transportation. The self-limited SSE thin films are evaluated in various ASS LMBs with different types of cathode (sulfur and lithium titanate) and anode materials (lithium and lithium-indium alloy) at both mold-cell and pouch-cell levels, demonstrating a stable performance and high-rate capability. This study provides a general strategy for the rational design of an SSE thin film towards high-energy-density ASS batteries.

1. Introduction

High-safety and high-energy-density batteries are urgently desired with the rapid growth of demands for electric vehicles, electronic devices, and grid energy storage.^[1] The limited energy density of commercial lithium-ion batteries severely retards the future application;^[2] whereas the developing high-energy-density batteries that, in general, comprise of lithium metal as the anode are producing worrisome safety concerns.^[3] All-solid-state (ASS) lithium metal batteries (LMBs) are strongly considered as the next-generation energy-storage devices due to their exceptional advantages in safety with eliminating the use of flammable organic electrolytes.^[4] Moreover, solid-state electrolytes (SSEs) as the key component in ASSLMBs hold the promise to cooperate with lithium metal anodes to construct

reliable electrochemical interfaces in working batteries towards expanded working voltage window and high energy density.^[5]

SSEs are generally classified into polymer electrolytes and inorganic electrolytes.^[1a,6] Polymer electrolytes own superior ductility that enables the application in flexible devices, but also low ionic conductivities (usually $<10^{-6} \text{ S cm}^{-1}$ at room temperature) and poor mechanical strength.^[7] On the contrary, a variety of inorganic electrolytes with high room-temperature ionic conductivity has been developed,^[4d,8] among which inorganic sulfide electrolytes are rather promising because of the high ionic conductivity that is comparable to that of a commercial liquid electrolyte ($>10^{-2} \text{ S cm}^{-1}$ at room temperature).^[1b,4a,9]

Despite the numerous efforts made so far in fundamental understanding of inorganic sulfide electrolytes,^[4c,10] the application of sulfide-based ASS batteries has been impeded mostly due to the practically low energy density of the whole device.^[11] The large proportion of inactive materials in the whole device, especially the thick SSE layer with a high apparent gravimetric density, is believed to be the major obstacle.^[7c,11b-d,12] Recently, Li et al. projected the energy density of ASS LMBs to the thickness of SSE.^[13] The thicknesses of at most 75 and 50 μm are necessitated for ASS LMBs with an energy density of 400 Wh kg^{-1} , utilizing sulfur and lithium cobalt oxide as the cathode, respectively. However, in usual processes, sulfide SSE powders are compacted into pellets, which exhibit a thickness of $>200 \mu\text{m}$ and are prone to crack.^[4b,12b,c] Moreover, it is difficult to scale up the powder pressing method to obtain large-area

Dr. G.-L. Zhu, Dr. C.-Z. Zhao, J.-K. Hu, Dr. H.-X. Nan, Dr. Y. Lu,
Dr. X.-Y. Liu, Prof. Q. Zhang
Beijing Key Laboratory of Green Chemical Reaction Engineering
and Technology Department of Chemical Engineering
Tsinghua University
Beijing 100084, China
E-mail: zhang-qiang@mails.tsinghua.edu.cn

Dr. G.-L. Zhu, Prof. H.-J. Peng
Institute of Fundamental and Frontier Sciences
University of Electronic Science and Technology of China
Chengdu 611731, China

Dr. G.-L. Zhu, Prof. C. He
College of Chemistry and Chemical Engineering
Shenzhen University
Shenzhen 518061, China

Dr. C.-Z. Zhao
State Key Laboratory of Automotive Safety and Energy
School of Vehicle and Mobility
Tsinghua University
Beijing 100084, China

Dr. H. Yuan, Prof. J.-Q. Huang
Advanced Research Institute of Multidisciplinary Science
Beijing Institute of Technology
Beijing 100081, China

Dr. J. Zhang
AAC Technologies Holdings Inc.
Nanjing 210093, China

 The ORCID identification number(s) for the author(s) of this article can be found under <https://doi.org/10.1002/adfm.202101985>.

DOI: 10.1002/adfm.202101985

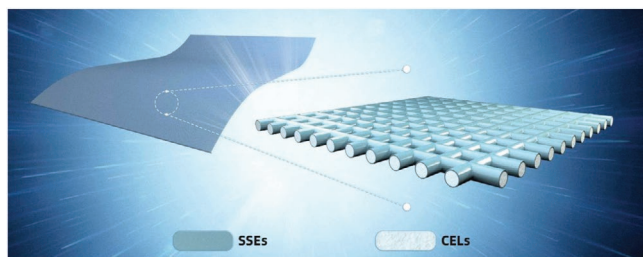


Figure 1. Schematic illustrations of the free-standing and flexible SSE film and the intercrossed CELs skeleton coated with a thin sulfide SSE layer to construct a 3D interconnecting ionic-conducting framework. SSEs represent the sulfide solid-state electrolytes, CELs represent the cellulose skeleton.

SSE films for bulk applications.^[5b,12a,14] Therefore, it is crucial and urgent to develop strategies for large-scale preparation of sulfide SSE thin films (<75 μm) with desirable ion-transport and mechanical properties.^[7c,11b-d,12]

In this contribution, a self-limited strategy is proposed to prepare ultrathin, free-standing, and flexible sulfide SSE films (**Figure 1**). Self-limited is that the sulfide SSE particles prefer to interact with the cellulose (CEL) fiber rather than themselves due to the strong reaction between the CEL and SSE particles. Thus, the thickness of SSE film will not increase with the increasing amount of casting slurry when the CEL was strongly wrapped by one layer of SSE particles. Finally, the thinness of the SSE film was defined by a pre-organized and thickness-designated porous substrate. The thin CEL skeleton

promises high mechanical strength, good flexibility, and excellent adhesion to sulfide particles to form continuous and stable ion transport channels in a working battery. The ASS LMBs with the free-standing SSE film and various cathode/anode combinations show excellent cycling performances and enhanced energy density at both mold-cell and pouch-cell levels.

2. Results and Discussion

As shown in Figure 1, herein we employed a cheap commodity CEL membrane as the skeleton. Argyrodite-type $\text{Li}_6\text{PS}_5\text{Cl}$ was selected for proof-of-concept due to its high intrinsic ionic conductivity at room temperature ($>10^{-3} \text{ S cm}^{-1}$). The SSE film was fabricated through a routine blade-coating technique that has been widely employed in the lithium ion battery industry (Figure S1, Supporting Information). **Figure 2a** shows a large piece of SSE film with a size of 32 mm \times 32 mm, indicating the ability of scaling up. In contrast, the cold-pressed SSE pellet is prone to crack, exhibiting poorer mechanical integrity at a macroscopic scale (Figure 2b). Microscopic texture of the SSE materials further reveals the difference in their structures. The SSE film exhibits a smooth surface consisting of closely packed sulfide particles along the direction of CEL fibers (Figure 2c). While in the SSE pellets, the connections between primary particles are loose, producing inter-particle porosity with a pore width of up to micrometers (Figure 2d). The denser integration of sulfide particles regulated by the CEL skeleton is believed to

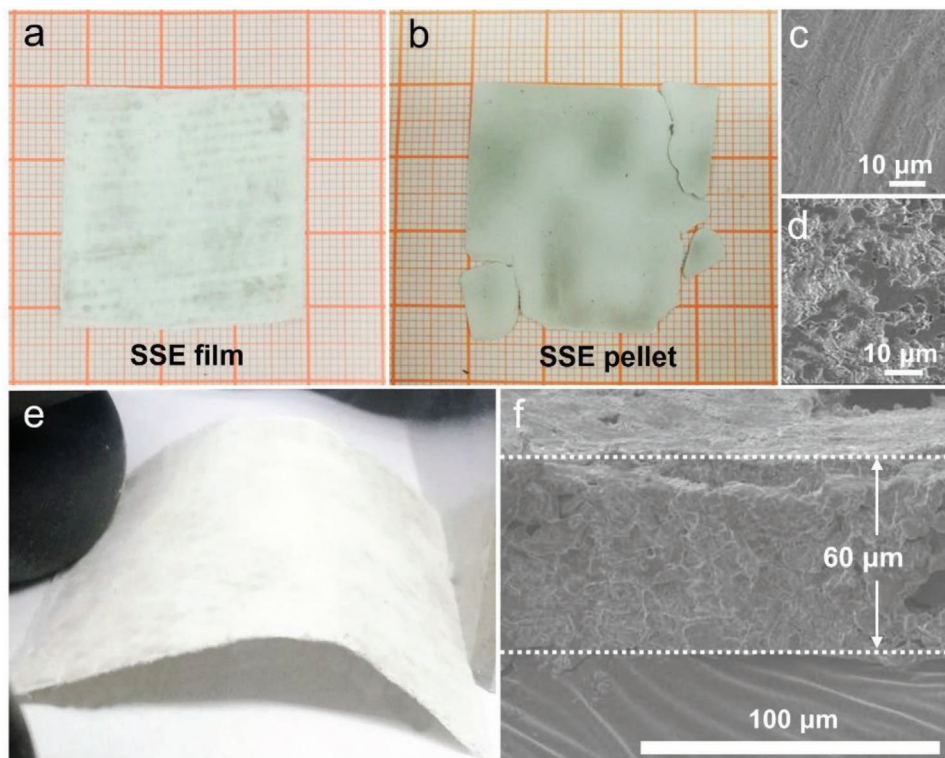


Figure 2. Morphological characterizations of the SSE film. Photo images and SEM images of (a,c) the SSE film and (b,d) the SSE pellet. e) Photograph of a flexible SSE film with a size of 30 mm \times 50 mm that is under mechanical deformation. f) Cross-section SEM image of the SSE film.

endow the SSE film superior flexibility under mechanical deformation and shows a tensile strength of 10.4 MPa (Figure S2a, Supporting Information), enabling the potential application of free-standing SSE films in flexible devices (Figure 2e). Here, the CEL skeleton as a mechanical support integrates the sulfide particles attached to cellulose fiber into a continuous and whole network, which greatly improves the mechanical strength of the SSE film. Besides, the CEL skeleton shows a tensile strength of 13.2 MPa (Figure S2b, Supporting Information). Therefore, the enhanced mechanical properties of SSE film are mainly attributed to the CEL skeleton.

Besides the macroscopic flexibility enabled by the pliable CEL skeleton, the thickness of the SSE film could be easily controlled by the thickness of the CEL skeleton. An ultrathin SSE film of 60 μm thick was obtained by limiting the thickness of the CEL skeleton to 29 μm (Figure 2f). Such a thickness is significantly lower than most of the reported sulfide-based SSEs, which is promising for enhancing the practical energy density of an ASSLMB. Interestingly, the thickness of the SSE film could be directly correlated to the thickness of the CEL skeleton (Figure S3, Supporting Information). The fitted linear correlation in Figure S3e, Supporting Information, reveals that: 1) engineering the thickness of the skeleton serves as a direct means of tuning the film thickness; 2) a slope close to one indicates the thickness of coating layer on one single CEL fiber being independent of the total thickness of the skeleton; and 3) an intercept of around 24 μm is attributed to the surface-tension-induced formation of slurry liquid film on top of the skeleton, which might be inevitable but also highly tunable through engineering the interfacial wetting properties to achieve a SSE film with even thinner thickness. Among the three features as revealed, the second one is of particular interest as it implies a “self-limited” assembly of sulfide particles on the CEL surface. The limited thickness of the coating layer restrains the final thickness of the SSE film after cold pressing.

To further elucidate the origin of above “self-limited” characteristic during slurry coating, the morphologies of CEL skeleton before and after slurry coating, as well as the chemical interactions between CEL and sulfide particles, were probed. The pristine CEL skeleton presents as a membrane weaved of warp and woof, providing both longitudinal and latitudinal mechanical supports to the free-standing SSE film (Figure S4a, Supporting Information). The diameter of a single CEL fiber increased from

16 \pm 4 to 23 \pm 5 μm after slurry coating (Figure S4b,c, Supporting Information). The increase in the diameter corresponds to a thickness of ca. 3–4 μm for the sulfide coating layer, approximating to the statistical mean diameter of sulfide particles. Such an accordance points to the hypothesis that sulfide particles prefer to interact with the CEL fiber rather than themselves. The strong interaction was evidenced by the X-ray photoelectron spectroscopy (Figure S5, Supporting Information). The characteristic peaks of the thiophosphate anion exhibit a blue shift of \approx 0.3 eV in binding energies of both S 2p and P 2p spectra from pristine $\text{Li}_6\text{PS}_5\text{Cl}$ to that in the SSE film (Figure S5a,b, Supporting Information). Simultaneously, the characteristic peak of the hydroxyl group in CEL also shows a similar blue shift in the O 1s spectra after the incorporation with $\text{Li}_6\text{PS}_5\text{Cl}$ particles. These blue shifts of binding energies indicated the electron lost from the hydroxyl group of CEL^[15] and may be accepted by the solvent, leading to the strong interaction between CEL and adhered sulfide particles. This is confirmed by Figure S4b,c, Supporting Information, the sulfide particles are tightly wrapped on the CEL fiber after slurry coating.

Through the construction of stable interface between CEL and sulfides, continuous and robust ion transport channels are realized in the composite SSE film. The ionic conductivity of the SSE film was evaluated by electrochemical impedance spectroscopy (EIS) at 25 $^\circ\text{C}$ (Figure S6, Supporting Information). The SSE film exhibits an ionic conductivity of 6.3 mS cm^{-1} , which is slightly lower than the cold-pressed SSE pellet (8.6 mS cm^{-1}) due to the incorporation of nonconducting CEL skeleton. The ionic impedance is calculated based on $R = L/\sigma \times A$ (L is the thickness of film, σ is the ionic conductivity, A is the area of electrolyte). However, owing to the sharp decrease in the thickness from 500 μm for the SSE pellet to 60 μm for the SSE film, a significant reduction in the bulk ion transport impedance from 45.8 to 14.6 Ω is achieved (Figure 3a). The significantly reduced bulk ionic impedance further evokes the rational design and fabrication of ultrathin SSEs in addition to the enhancement in projected energy density, laying the foundation towards safe, high-energy-density, and fast-charging ASSLMBs.

The X-ray diffraction (XRD) pattern of the SSE film shows a number of intense diffraction peaks indexed to the argyrodite $\text{Li}_6\text{PS}_5\text{Cl}$ crystal structure (Figure 3b).^[2d,3f,8b] The peak intensities are comparable to those of pristine $\text{Li}_6\text{PS}_5\text{Cl}$ particles. Moreover, the XRD patterns of other phases were not detected

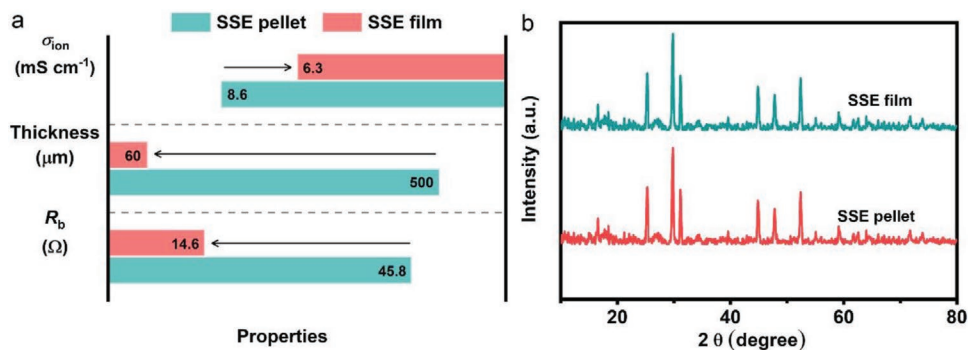


Figure 3. Properties and structure of the SSE electrolytes. a) Comparison of ionic conductivity (σ_{ion}), thickness, and bulk resistance (R_b) between the SSE film and the SSE pellet. b) XRD patterns of the SSE film and the SSE pellet.

in the SSE film. All these evidences indicate that incorporating the CEL skeleton in the $\text{Li}_6\text{PS}_5\text{Cl}$ -based SSE film did not alter the phase structure neither the grain size of $\text{Li}_6\text{PS}_5\text{Cl}$. In summary, the “self-limited” assembly of sulfide particles on the CEL surface leading a thinner final thickness of the SSE film, and constructing a continuous and robust ion transport channels in the SSE film, which shows a higher ionic conductivity and mechanical property in comparison with other woks (Table S1, Supporting Information).^[16]

ASS lithium–sulfur batteries (LSBs) are regarded to completely eliminate the formation of polysulfide soluble in conventional liquid electrolytes and thus avoid the notorious “shuttle effect” found to lower the sulfur utilization and shorten the cycling life of liquid-electrolyte LSBs.^[17] In this sense, the merits of the free-standing SSE film such as ultrathinness, excellent robustness, and high ionic conductivity were utilized for ASS LSBs assembled in a mechanical mold, where a lithium–indium (LiIn) alloy anode was employed to stabilize the anodic interface (Figure 4a).

As shown in Figure 4b, the mold cell of ASS LSB with a SSE film as the electrolyte delivers an initial discharge capacity of 1270 mAh g^{-1} at 0.1 C ($1 \text{ C} = 1672 \text{ mAh g}^{-1}$) and the discharge capacity still remains 84% of initial capacity after 100 cycles. Besides, a high Coulombic efficiency of 99.9% sustains upon cycling, indicating the “shuttle-free” feature of the ASS LSB. Such a superior stability and a high specific capacity are comparable to or even slightly better than the ASS LSB cell with a cold-pressed SSE pellet. Considering the greatly reduced thickness from the SSE pellet to the SSE film, the stable performance of the SSE film in an ASS LSB is expected to be more appealing for practical applications that demand for high energy density and high safety.

Note that a current rate of 0.1 C is not sufficiently high to touch the limit of ionic conductivity. To further investigate the capability of the SSE film for fast-charging batteries, galvanostatic tests under various current rates were conducted (Figure 4c,d). The charge/discharge profiles of ASS LSBs exhibit a single-plateau of $\approx 2.1 \text{ V}$ versus Li^+/Li , which suggests that the electrochemical reaction corresponding to a solid-phase conversion mechanism of $\text{S} + 2\text{Li}^+ + 2\text{e}^- \leftrightarrow \text{Li}_2\text{S}$ occurs in all-solid-state cells^[9b,18] (Figure 4c). In addition, the polarization of ASS LSB with a SSE film is around 0.42 V at 0.5 C , which is lower than 0.51 V for the cell with a cold-pressed SSE pellet. The mitigated cell polarization is attributed to the rapid ion transport within the 3D continuous sulfide pathways built in the SSE film. The stable interface between sulfides and CEL also contributes to the high stability of ionic-conducting framework under high current densities. With increasing current density from 0.05 to $0.1, 0.2,$ and 0.5 C , unprecedented reversible capacities of $1311, 1266, 1199,$ and 1008 mAh g^{-1} are maintained, respectively (Figure 4d). After reversing the current density back to 0.05 C , a discharge capacity of 1305 mAh g^{-1} is recovered. In contrast, the ASS LSB with a cold-pressed SSE pellet delivers lower reversible capacities at various C-rates. Specifically, at 0.5 C , the capacity is only 673 mAh g^{-1} , 33% lower than that of the ASS LSB with a SSE film, and only 85% of the initial capacity (1272 mAh g^{-1}) is recovered once the current density set back to 0.05 C . Besides the higher reversible capacities at high rates, the SSE film also enables higher energy efficiency of an ASS LSB in comparison with the SSE pellet, which is critical for reducing the joule heat generated in the ASS batteries toward higher intrinsic safety (Figure 4d). Overall, decreasing the thickness of a SSE layer not only benefits a high energy density but also allows fast-charging capability for an ASS battery.

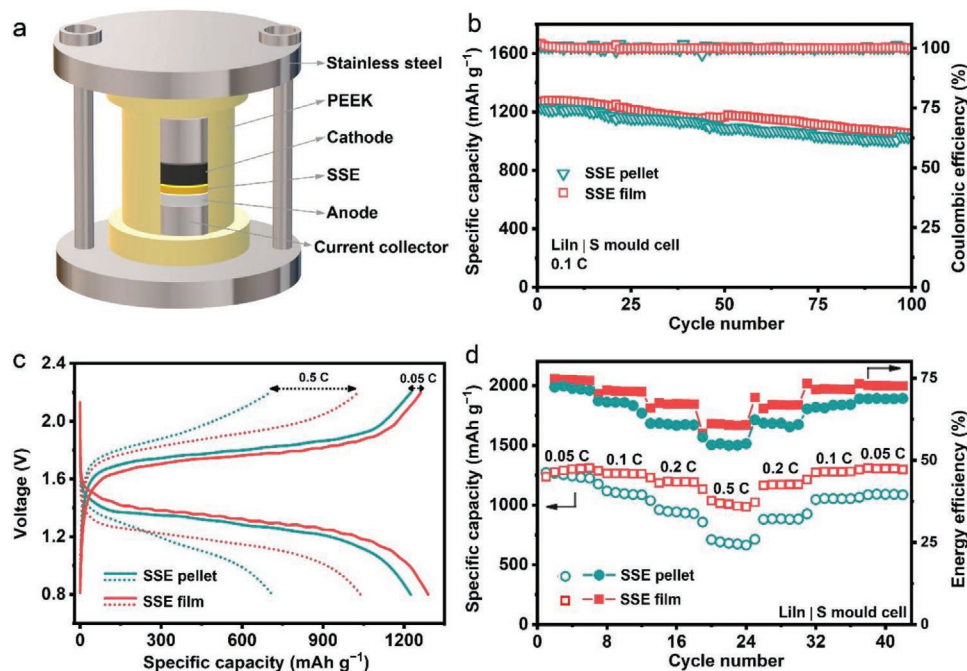


Figure 4. Electrochemical performances of the SSEs evaluated in mold cells. a) Schematic diagram of the LiIn | S mould cell. b) Cycling performance at 0.1 C , c) galvanostatic charge–discharge profiles at 0.05 and 0.5 C , and d) rate performances of LiIn | S cells with the SSE film and the SSE pellet.

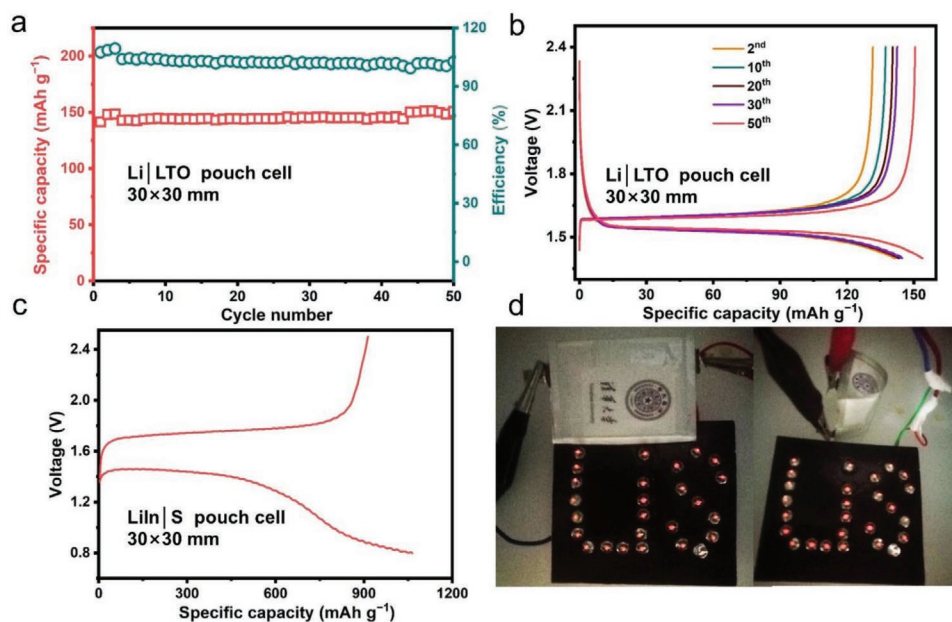


Figure 5. Electrochemical performances of the SSEs evaluated in pouch cells. a) Cycling performance and b) charge–discharge profiles of an ASS Li | LTO pouch cell at 0.1 C. c) Charge–discharge profiles of ASS LiIn | S pouch cell at 0.05 C. d) ASS LiIn | S pouch cell to illuminate an array of light-emitting diodes at a flat or a bended state.

To demonstrate the versatility of the SSE film for practical applications, ASS LMB pouch cells were assembled. Compared with the mold cell, the pouch cell is 10–50 times larger and operated with much smaller external pressure (5–10 kPa in pouch cell, 2–5 MPa in mold cell), and thus a more appropriate platform for evaluating the SSEs in near-practical conditions. Nevertheless, the large size of pouch cell also strives for higher requirements on the processability and ion transport ability of a large-area SSE layer. Owing to the structural stability, lithium titanate ($\text{Li}_4\text{Ti}_5\text{O}_{12}$, LTO) was first selected as the working electrode paired with the lithium anode in an ASS pouch cell (30 mm \times 30 mm) using a large piece of SSE film as the electrolyte. The Li | LTO pouch cell delivers an initial discharge capacity of 148 mAh g^{-1} at 0.1 C and exhibits excellent stability with 100% capacity retention and a 99% Coulombic efficiency during 50 cycles (Figure 5a). The charge/discharge profiles show negligible capacity degradation and low polarization, suggesting the high compatibility of the SSE film with lithium metal anode in a practical pouch cell (Figure 5b). In addition, ASS LiIn | S pouch cells with the same size of 30 mm \times 30 mm and a high areal capacity of 4.2 mAh cm^{-2} were also assembled. As shown in Figure 5c, the ASS LiIn | S pouch cell delivers a high initial discharge capacity of 1064 mAh g_s^{-1} (0.03 Ah) at 0.05 C. Also, the light-emitting diodes can be illuminated by the ASS LiIn | S pouch cell even after bending, demonstrating the great flexibility enabled by the SSE film (Figure 5d).

Finally, it is crucial to evaluate the effect of the SSE film on enhancing the energy density of the whole device. The achievable specific energy is calculated from the product of active material loading, active material utilization, and average cell voltage, divided by the total weight of all cell components.^[17f] The specific parameters are shown in Table S2, Supporting Information. With the reduction of thickness layer from

500 (pellet) to 60 μm (the free-standing SSE film), the gravimetric energy density of an ASS LSB drastically increases from 108 to 394 Wh kg^{-1} . The free-standing sulfide SSE film enabled by a self-limited strategy paves an avenue to realize high-energy-density and high-safety ASS LMBs for both routine applications and flexible devices. Considering the lower sulfur loading (2.5 mg cm^{-2}) than what we estimated in Table S1, Supporting Information (5.0 mg cm^{-2}) to access the high projected energy density of 394 Wh kg^{-1} for ASS LMBs it requires more works on improving the active material loading and interface stability in the future.

3. Conclusions

A self-limited strategy was developed for the fabrication of ultrathin, free-standing, and flexible sulfide-based SSE films. A mechanically pliable and chemical compatible CEL skeleton was designed to shape the as-obtained SSE film with thinness and reinforce the SSE for high durability. Owing to the self-limited assembly of solid particles on the skeleton, as well as the intact interface, the SSE film was endowed with superior processability, thin thickness, flexibility, and a 3D interconnected ionic-conducting framework. A thin thickness of 60 μm was achieved, largely contributing to lowering the bulk resistance and mass of inactive SSE layer. With the free-standing SSE film, the ASS LiIn | S mold cell showed superior rate performances and delivered an unprecedented reversible capacity of 1008 mAh g^{-1} at 0.5 C. More importantly, the SSE film also showed excellent compatibility to various cathode/anode materials in ASS LMB pouch cells. This work demonstrates an effective strategy of designing an ultrathin SSE film without sacrificing the mechanical and ion-transport performances and

offers a promising route towards safe, high-energy-density, and fast-charging ASS batteries.

Supporting Information

Supporting Information is available from the Wiley Online Library or from the author.

Acknowledgements

This work was supported by Beijing Municipal Natural Science Foundation (Z20J00043), National Natural Science Foundation of China (21808124, 21825501, 22005200, and U1801257), National Key Research and Development Program (2016YFA0200102 and 2016YFA0202500), and Tsinghua University Initiative Scientific Research Program. C.-Z.Z. and Y.L. appreciate the Shuimu Tsinghua Scholar Program of Tsinghua University.

Conflict of Interest

The authors declare no conflict of interest.

Data Availability Statement

Data available on request from the authors.

Keywords

all-solid-state batteries, lithium metal batteries, pouch cells, solid-state electrolyte thin films, sulfide electrolytes

Received: February 26, 2021

Revised: April 23, 2021

Published online: June 4, 2021

- [1] a) R. Chen, Q. Li, X. Yu, L. Chen, H. Li, *Chem. Rev.* **2020**, *120*, 6820; b) S. Randau, D. A. Weber, O. Kötz, R. Koerver, P. Braun, A. Weber, E. Ivers-Tiffée, T. Adermann, J. Kulisch, W. G. Zeier, F. H. Richter, J. Janek, *Nat. Energy* **2020**, *5*, 259; c) M. Winter, B. Barnett, K. Xu, *Chem. Rev.* **2018**, *118*, 11433; d) Y. Liang, C.-Z. Zhao, H. Yuan, Y. Chen, W. Zhang, J.-Q. Huang, D. Yu, Y. Liu, M.-M. Titirici, Y.-L. Chueh, H. Yu, Q. Zhang, *InfoMat* **2019**, *1*, 6; e) L. Li, Y. Deng, G. Chen, *J. Energy Chem.* **2020**, *50*, 154; f) Y. Kato, S. Hori, T. Saito, K. Suzuki, M. Hirayama, A. Mitsui, M. Yonemura, H. Iba, R. Kanno, *Nat. Energy* **2016**, *1*, 16030.
- [2] a) Y. Zhang, Y. Shi, X.-C. Hu, W.-P. Wang, R. Wen, S. Xin, Y.-G. Guo, *Adv. Energy Mater.* **2020**, *10*, 1903325; b) J. Lee, K. Lee, T. Lee, H. Kim, K. Kim, W. Cho, A. Coskun, K. Char, J. W. Choi, *Adv. Mater.* **2020**, *32*, 2001702; c) M. He, Z. Cui, F. Han, X. Guo, *J. Alloys Compd.* **2018**, *762*, 157; d) C. Yu, S. Ganapathy, E. R. H. van Eck, L. van Eijck, S. Basak, Y. Liu, L. Zhang, H. W. Zandbergen, M. Wagemaker, *J. Mater. Chem. A* **2017**, *5*, 21178; e) D. Cao, Y. Zhang, A. M. Nolan, X. Sun, C. Liu, J. Sheng, Y. Mo, Y. Wang, H. Zhu, *Nano Lett.* **2019**, *20*, 1483.
- [3] a) F. Mizuno, A. Hayashi, K. Tadanaga, M. Tatsumisago, *Adv. Mater.* **2005**, *17*, 918; b) H.-J. Deiseroth, S.-T. Kong, H. Eckert, J. Vannahme, C. Reiner, T. Zaiß, M. Schlosser, *Angew. Chem., Int. Ed.* **2008**, *47*, 755; c) Y. Zhu, Y. Mo, *Angew. Chem., Int. Ed.* **2020**, *59*, 17472; d) Y. E. Choi, K. H. Park, D. H. Kim, D. Y. Oh, H. R. Kwak, Y.-G. Lee, Y. S. Jung, *ChemSusChem* **2017**, *10*, 2605; e) X. Li, J. Liang, J. Luo, M. N. Banis, C. Wang, W. Li, S. Deng, C. Yu, F. Zhao, Y. Hu, T.-K. Sham, L. Zhang, S. Zhao, S. Lu, H. Huang, R. Li, K. R. Adair, X. Sun, *Energy Environ. Sci.* **2019**, *12*, 2665; f) S. Yubuchi, S. Teragawa, K. Aso, K. Tadanaga, A. Hayashi, M. Tatsumisago, *J. Power Sources* **2015**, *293*, 941.
- [4] a) G.-L. Zhu, C.-Z. Zhao, H. Yuan, B.-C. Zhao, L.-P. Hou, X.-B. Cheng, H.-X. Nan, Y. Lu, J. Zhang, J.-Q. Huang, Q.-B. Liu, C.-X. He, Q. Zhang, *Energy Storage Mater.* **2020**, *31*, 267; b) H. Yuan, H.-X. Nan, C.-Z. Zhao, G.-L. Zhu, Y. Lu, X.-B. Cheng, Q.-B. Liu, C.-X. He, J.-Q. Huang, Q. Zhang, *Batteries Supercaps* **2020**, *3*, 596; c) C.-Z. Zhao, B.-C. Zhao, C. Yan, X.-Q. Zhang, J.-Q. Huang, Y. Mo, X. Xu, H. Li, Q. Zhang, *Energy Storage Mater.* **2019**, *24*, 75; d) X.-B. Cheng, R. Zhang, C.-Z. Zhao, Q. Zhang, *Chem. Rev.* **2017**, *117*, 10403.
- [5] a) H. Liu, X.-B. Cheng, J.-Q. Huang, H. Yuan, Y. Lu, C. Yan, G.-L. Zhu, R. Xu, C.-Z. Zhao, L.-P. Hou, C. He, S. Kaskel, Q. Zhang, *ACS Energy Lett.* **2020**, *5*, 833; b) D. H. S. Tan, E. A. Wu, H. Nguyen, Z. Chen, M. A. T. Marple, J.-M. Doux, X. Wang, H. Yang, A. Banerjee, Y. S. Meng, *ACS Energy Lett.* **2019**, *4*, 2418; c) F. Han, A. S. Westover, J. Yue, X. Fan, F. Wang, M. Chi, D. N. Leonard, N. J. Dudney, H. Wang, C. Wang, *Nat. Energy* **2019**, *4*, 187; d) C.-Z. Zhao, X.-Q. Zhang, X.-B. Cheng, R. Zhang, R. Xu, P.-Y. Chen, H.-J. Peng, J.-Q. Huang, Q. Zhang, *Proc. Natl. Acad. Sci. U. S. A.* **2017**, *114*, 11069; e) C.-Z. Zhao, H. Duan, J.-Q. Huang, J. Zhang, Q. Zhang, Y.-G. Guo, L.-J. Wan, *Sci. China Chem.* **2019**, *62*, 1286; f) G.-L. Zhu, C.-Z. Zhao, J.-Q. Huang, C. He, J. Zhang, S. Chen, L. Xu, H. Yuan, Q. Zhang, *Small* **2019**, *15*, 1805389.
- [6] a) Y. Gao, A. M. Nolan, P. Du, Y. Wu, C. Yang, Q. Chen, Y. Mo, S.-H. Bo, *Chem. Rev.* **2020**, *120*, 5954; b) S. Chen, D. Xie, G. Liu, J. P. Mwizerwa, Q. Zhang, Y. Zhao, X. Xu, X. Yao, *Energy Storage Mater.* **2018**, *14*, 58; c) J. Janek, W. G. Zeier, *Nat. Energy* **2016**, *1*, 16141; d) Y. S. Jung, D. Y. Oh, Y. J. Nam, K. H. Park, *Isr. J. Chem.* **2015**, *55*, 472.
- [7] a) H. Huo, Y. Chen, J. Luo, X. Yang, X. Guo, X. Sun, *Adv. Energy Mater.* **2019**, *9*, 1804004; b) C.-W. Nan, L. Fan, Y. Lin, Q. Cai, *Phys. Rev. Lett.* **2003**, *91*, 266104; c) I. Villaluenga, K. H. Wujcik, W. Tong, D. Devaux, D. H. C. Wong, J. M. DeSimone, N. P. Balsara, *Proc. Natl. Acad. Sci. U. S. A.* **2016**, *113*, 52.
- [8] a) N. Sun, Q. Liu, Y. Cao, S. Lou, M. Ge, X. Xiao, W.-K. Lee, Y. Gao, G. Yin, J. Wang, X. Sun, *Angew. Chem., Int. Ed.* **2019**, *58*, 18647; b) C. Yu, L. van Eijck, S. Ganapathy, M. Wagemaker, *Electrochim. Acta* **2016**, *215*, 93.
- [9] a) N. Kamaya, K. Homma, Y. Yamakawa, M. Hirayama, R. Kanno, M. Yonemura, T. Kamiyama, Y. Kato, S. Hama, K. Kawamoto, A. Mitsui, *Nat. Mater.* **2011**, *10*, 682; b) F. Han, T. Gao, Y. Zhu, K. J. Gaskell, C. Wang, *Adv. Mater.* **2015**, *27*, 3473.
- [10] a) Y. Mo, S. P. Ong, G. Ceder, *Chem. Mater.* **2012**, *24*, 15; b) Y. Seino, T. Ota, K. Takada, A. Hayashic, M. Tatsumisagoc, *Energy Environ. Sci.* **2014**, *7*, 627; c) X. He, Y. Zhu, Y. Mo, *Nat. Commun.* **2017**, *8*, 15893; d) Y. Wang, W. D. Richards, S. P. Ong, L. J. Miara, J. C. Kim, Y. Mo, G. Ceder, *Nat. Mater.* **2015**, *14*, 1026; e) L.-P. Hou, H. Yuan, C.-Z. Zhao, L. Xu, G.-L. Zhu, H.-X. Nan, X.-B. Cheng, Q.-B. Liu, C.-X. He, J.-Q. Huang, Q. Zhang, *Energy Storage Mater.* **2020**, *25*, 436.
- [11] a) L. Xu, Y. Lu, C.-Z. Zhao, H. Yuan, G.-L. Zhu, L.-P. Hou, Q. Zhang, J.-Q. Huang, *Adv. Energy Mater.* **2021**, *11*, 2002360; b) S. Wang, X. Zhang, S. Liu, C. Xin, C. Xue, F. Richter, L. Li, L. Fan, Y. Lin, Y. Shen, J. Janek, C.-W. Nan, *J. Materiomics* **2019**, *6*, 70; c) K. Lee, S. Kim, J. Park, S. H. Park, A. Coskun, D. S. Jung, W. Cho, J. W. Choi, *J. Electrochem. Soc.* **2017**, *164*, A2075; d) Y. J. Nam, S. J. Cho, D. Y. Oh, J. M. Lim, S. Y. Kim, J. H. Song, Y. G. Lee, S. Y. Lee, Y. S. Jung, *Nano Lett.* **2015**, *15*, 3317.

- [12] a) X. Chen, W. He, L.-X. Ding, S. Wang, H. Wang, *Energy Environ. Sci.* **2019**, *12*, 938; b) Z. Jiang, S. Wang, X. Chen, W. Yang, X. Yao, X. Hu, Q. Han, H. Wang, *Adv. Mater.* **2020**, *32*, 1906221; c) J. Wan, J. Xie, X. Kong, Z. Liu, K. Liu, F. Shi, A. Pei, H. Chen, W. Chen, J. Chen, X. Zhang, L. Zong, J. Wang, L.-Q. Chen, J. Qin, Y. Cui, *Nat. Nanotechnol.* **2019**, *14*, 705.
- [13] L. Liu, J. Xu, S. Wang, F. Wu, H. Li, L. Chen, *eTransportation* **2019**, *1*, 100010.
- [14] a) F. J. Simon, M. Hanauer, A. Henss, F. H. Richter, J. Janek, *ACS Appl. Mater. Interfaces* **2019**, *11*, 42186; b) M. Yan, J.-Y. Liang, T.-T. Zuo, Y.-X. Yin, S. Xin, S.-J. Tan, Y.-G. Guo, L.-J. Wan, *Adv. Funct. Mater.* **2020**, *30*, 1908047; c) R. Xu, X.-B. Cheng, C. Yan, X.-Q. Zhang, Y. Xiao, C.-Z. Zhao, J.-Q. Huang, Q. Zhang, *Matter* **2019**, *1*, 317.
- [15] E. J. Foster, R. J. Moon, U. P. Agarwal, M. J. Bortner, J. Bras, S. Camarero-Espinosa, K. J. Chan, M. J. D. Clift, E. D. Cranston, S. J. Eichhorn, D. M. Fox, W. Y. Hamad, L. Heux, B. Jean, M. Korey, W. Nieh, K. J. Ong, M. S. Reid, S. Renneckar, R. Roberts, J. A. Shatkin, J. Simonsen, K. Stinson-Bagby, N. Wanasekara, J. Youngblood, *Chem. Soc. Rev.* **2018**, *47*, 2609.
- [16] a) C. Wang, D. Huang, S. Li, J. Yu, M. Zhu, N. Liu, Z. Lu, *Nano Lett.* **2020**, *20*, 7397; b) Y. J. Nam, D. Y. Oh, S. H. Jung, Y. S. Jung, *J. Power Sources* **2018**, *375*, 93; c) J. Wu, L. Yuan, W. Zhang, Z. Li, X. Xie, Y. Huang, *Energy Environ. Sci.* **2021**, *14*, 12.
- [17] a) H.-J. Peng, Z.-W. Zhang, J.-Q. Huang, G. Zhang, J. Xie, W.-T. Xu, J.-L. Shi, X. Chen, X.-B. Cheng, Q. Zhang, *Adv. Mater.* **2016**, *28*, 9551; b) X. Yao, N. Huang, F. Han, Q. Zhang, H. Wan, J. P. Mwizerwa, C. Wang, X. Xu, *Adv. Energy Mater.* **2017**, *7*, 1602923; c) Q. Zhang, D. Cao, Y. Ma, A. Natan, P. Aurora, H. Zhu, *Adv. Mater.* **2019**, *31*, 1901131; d) K. Kisu, S. Kim, R. Yoshida, H. Oguchi, N. Toyama, S.-i. Orimo, *J. Energy Chem.* **2020**, *50*, 424; e) Q. Zhang, N. Huang, Z. Huang, L. Cai, J. Wu, X. Yao, *J. Energy Chem.* **2020**, *40*, 151; f) B. D. McCloskey, *J. Phys. Chem. Lett.* **2015**, *6*, 4581.
- [18] a) H. Nagata, Y. Chikusa, *J. Power Sources* **2014**, *264*, 206; b) M. Nagao, A. Hayashi, M. Tatsumisago, *J. Mater. Chem.* **2012**, *22*, 10015; c) M. Nagao, A. Hayashi, M. Tatsumisago, *Energy Technol.* **2013**, *1*, 186; d) Z. Lin, Z. Liu, N. J. Dudney, C. Liang, *ACS Nano* **2013**, *7*, 2829; e) X. Yao, D. Liu, C. Wang, P. Long, G. Peng, Y.-S. Hu, H. Li, L. Chen, X. Xu, *Nano Lett.* **2016**, *16*, 7148; f) L. Chen, L. Z. Fan, *Energy Storage Mater.* **2018**, *15*, 37.